

## Mechanical and biological evaluation of 3D printed 10CeTZP-Al<sub>2</sub>O<sub>3</sub> structures

Lidia Goyos-Ball<sup>a, b\*</sup>, Esther García-Tuñón<sup>c</sup>, Elisa Fernández<sup>a</sup>, Raquel Díaz<sup>a</sup>, Adolfo Fernández<sup>a, b</sup>, Catuxa Prado<sup>a</sup>, Eduardo Saiz<sup>c</sup> and Ramón Torrecillas<sup>a, d</sup>.

\* Corresponding author.

E-mail addresses: l.goyos@cinn.es, lidiagoyos@gmail.com (Lidia Goyos-Ball)

- a. *Nanomaterials and Nanotechnology Research Centre (CINN). Avenida de la Vega, 4-6. 33940 El Entrego, Asturias, Spain*
- b. *Nanoker Research, Pol. Ind. Olloniego, Parcela 22A, Nave 5, 33660 Oviedo, Spain*
- c. *Department of Materials of Imperial College London. Royal School of Mines. Exhibition Road. SW7 2AZ London, UK*
- d. *Moscow State University of Technology "STANKIN". Vadkovskij per. 1, Moscow, Moscow Oblast, Russia*

### ABSTRACT

Three-dimensional structures were robocasted from a 10 mol% ceria-stabilized zirconia and alumina composite (10CeTZP-Al<sub>2</sub>O<sub>3</sub>). A hydrogel-based printable ink was developed using a unique non-ionic copolymer surfactant. Self-supporting and free-standing structures, including round lattices with interconnected pores (200-600 μm pores; 30-50% porosity), rectangular bars (95 % density on average) and cones were successfully printed. The round lattices of 200 μm pores and 30% porosity showed compression strengths similar to those of cortical bone, reaching almost 200 MPa. The maximum flexural strength value attained for the rectangular bars was 575 MPa. In vitro biological studies demonstrated that the samples allow for practically 100% cell viability, confirming their non-cytotoxic nature. Cell differentiation tests were performed using osteoblasts incubated for 7 days in supplemented cell culture medium. Quantification of specific osseous differentiation genes showed that the robocasted structures induced a higher degree of osseous differentiation than tissue culture polystyrene.

**Keywords:** 3D printing, robocasting, ceramic composites, scaffolds, osseous differentiation

## 1. Introduction

Artificial devices fabricated from biomaterials have saved and improved millions of lives to date [1,2]. In upcoming years the need for biomaterials will increase exponentially, mainly due to a continuously ageing population [3,4]. In terms of bone related diseases, in particular, the development of biomaterials with enhanced mechanical properties and tailored osseo-stimulative designs [5,6] and the improvement of current scaffold manufacturing techniques are urgently required to cope with current and future clinical demands [7,8].

The biomedical field has evolved and expanded in all directions in the search for the ideal bone scaffold, covering many different types of materials: from metals and calcium phosphates to other ceramics, bioglasses, composites, organic/inorganic hybrid networks, [9-15] etc. In this regard, ceramic materials, such as zirconia ( $ZrO_2$ ) and alumina ( $Al_2O_3$ ), are gaining importance due to their biocompatibility, aesthetics, mechanical properties and negligible ion release.

In general, ceramic materials are brittle and have virtually no plasticity; however, there are exceptions, such as ceria-stabilized zirconia (CeTZP), which presents an important intrinsic reinforcement mechanism associated to its phase transformation, called transformation toughening [16]. Throughout this work we study a ceria-stabilized zirconia and alumina composite ( $10CeTZP-Al_2O_3$ ) which, as a ceramic biomaterial, resists corrosion and wear and has high chemical stability. Furthermore, it has better fracture toughness and ageing properties than conventional yttria-stabilized  $ZrO_2$  and shows enhanced mechanical performance when compared to monolithic  $Al_2O_3$  [17-21]. CeTZP itself has high fracture toughness but low flexural strength [22]; the dispersed  $Al_2O_3$  phase suppresses grain growth and increases the composite's strength without affecting its fracture toughness [17,23,24]. This material's superior fracture toughness is due to its stress-induced martensitic transformation [25,26].

Ceramic scaffolds with controlled 3D architectures are essential in biomedical applications that imply taking specific structural requirements into account, such as having sufficient open and interconnected porosity to allow for bone tissue formation and vascularization and achieving a precise compromise between scaffold porosity and strength [14]. Robocasting is an additive manufacturing technique that offers the possibility to rapidly create complex structures with controlled morphologies, following a pre-designed digital model, via a layer-by-layer deposition process. It is gaining ground over conventional production methods in circumstances that require short or individual production series, tailored sizes, intricate shapes, controlled porosity, etc.

Up to date, most additive manufacturing (AM) techniques have focused on certain metallic and polymeric materials, whereas 3D printing of ceramic components has been very limited. In terms of research, ceramics have been used in robocasting for more than a decade; however, printing ceramics still implies challenges such as developing simple-to-formulate inks of appropriate composition, flow consistency and behaviour and viscoelastic properties. Ceramic inks for 3D printing must contain a high solids volume fraction to minimize shrinkage during drying and thus resist the involved capillary stresses [27-29]. They must also be shear thinning, to flow through very narrow

deposition nozzles, and have a predominant elastic behaviour, to recover their initial structure immediately after deposition while maintaining their filament shape, bonding to the underlying layer and supporting the weight of the successive layers [27-31]. Using water as a means of formulation in these thermo-responsive inks provides multiple advantages, especially in comparison to organic solvent-based alternatives [27]. These inks are relatively simple, clean, non-toxic, low-cost and easily up-scalable. Additionally, the use of hydrogel-based ceramic inks avoids both the need to closely control the pH and the use of additives [27,28,30,32]. The use of a non-ionic polyethylene oxide and polypropylene oxide copolymer surfactant, Pluronic F-127, is becoming a common approach in robocasting due to its unique thermal behaviour. Pluronic in water below  $\sim 17^{\circ}\text{C}$  - at concentrations above  $\sim 15\text{ wt\%}$  - behaves like a low viscosity liquid, but when the temperature rises above  $\sim 17^{\circ}\text{C}$  it changes conformation, forming micelles that result in a highly viscous gel [30]. This behaviour is very convenient for printing at room temperature and ideal for ceramic materials such as calcium phosphates or glasses, as demonstrated in previous studies [28,30,32].

Taking all of the above into account, the main objectives of the present work are to print robust dense and porous  $10\text{CeTZP-Al}_2\text{O}_3$  structures using a hydrogel-based ceramic ink and prove their mechanical and biological suitability for load-bearing applications within the biomedical field.

## 2. Materials and methods

### 2.1 Ceramic ink formulation, production and printing

**Ink preparation.** A printable ceramic ink was attained by mixing 10CeTZP-Al<sub>2</sub>O<sub>3</sub> powder (35 vol%), prepared by following a patented colloidal synthesis route [33] and sieved below <15 μm, and an aqueous solution of Pluronic® F-127 by Sigma Aldrich (25 wt% in deionized water at 4°C). The Pluronic® F-127 solution components were mixed at 2000 rpm for 6 min and degassed at 1000 rpm for 4 min using a Thinky ARE-250 planetary mixer, they were then refrigerated at 4°C for 24 h to allow for bubble dissipation. The ceramic ink constituents were mixed at 2000 rpm for 15 min and degassed at 1000 rpm for 15 min using the same apparatus.

**Ink rheology.** The flow behaviour and viscoelastic properties of the Pluronic® F-127 solution and the ceramic ink were measured using a Discovery Hybrid Rheometer HR1 (TA Instruments) equipped with a parallel plate ( $\varnothing = 40$  mm) and a solvent trap cover. Flow behaviour was measured applying a flow ramp (viscosity vs. shear rate). The viscoelastic properties (storage modulus, G', and loss modulus, G'') were assessed with strain and frequency sweeps; in detail, with stress-controlled amplitude sweeps (from 0.01 % to 10 %) at a fixed frequency of 1.0 Hz, and stress-controlled frequency sweeps (from 0.1 Hz to 100 Hz) at a fixed strain of 0.1 %. The effect of temperature was monitored by applying a temperature ramp at fixed strain and frequency.

**Printing.** 3D structures were printed using a robotic assisted deposition device (3-D Inks, Stillwater, OK). Robocad 4.0 software was used to design the 3D structures and to configure and operate the printing equipment. The ink was placed in 3 cm<sup>3</sup> syringes and extruded through conical tips of 580 μm in diameter at a speed of 6 mm/s, which allowed for a continuous and stable flow. A wide range of 3D structures were printed on both porous (newspaper, sieves) and non-porous (teflon) substrates and in different media (air and oil). The optimised ink was used to build dense rectangular test bars for mechanical strength evaluation, round lattices with interconnected pores for biological assaying and conically shaped structures (Fig. 1). Two main patterns were applied when designing the round lattices: a) the simple round lattice pattern (Fig. 2a and Fig. 2c), and b) the complex round lattice pattern, consisting of an ABAB type configuration (Fig. 2b and Fig. 2d). The round lattices were designed to have final pore sizes between 200-800 μm, previously reported as optimal for bone tissue growth [13,14,34].

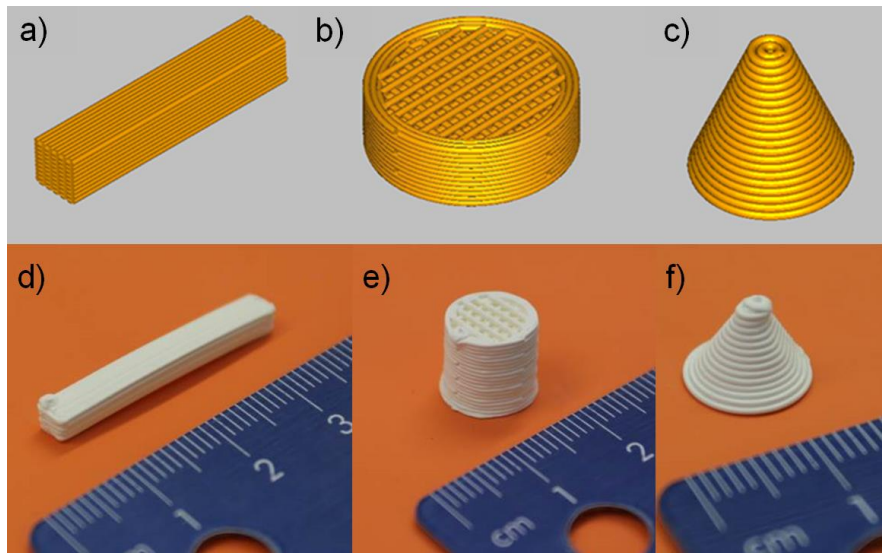


**Fig. 1:** 3D designs: (a) rectangular bar, (b) round lattice and (c) cone, and printed structures: (d) rectangular bar, (e) round lattice and (f) cone.

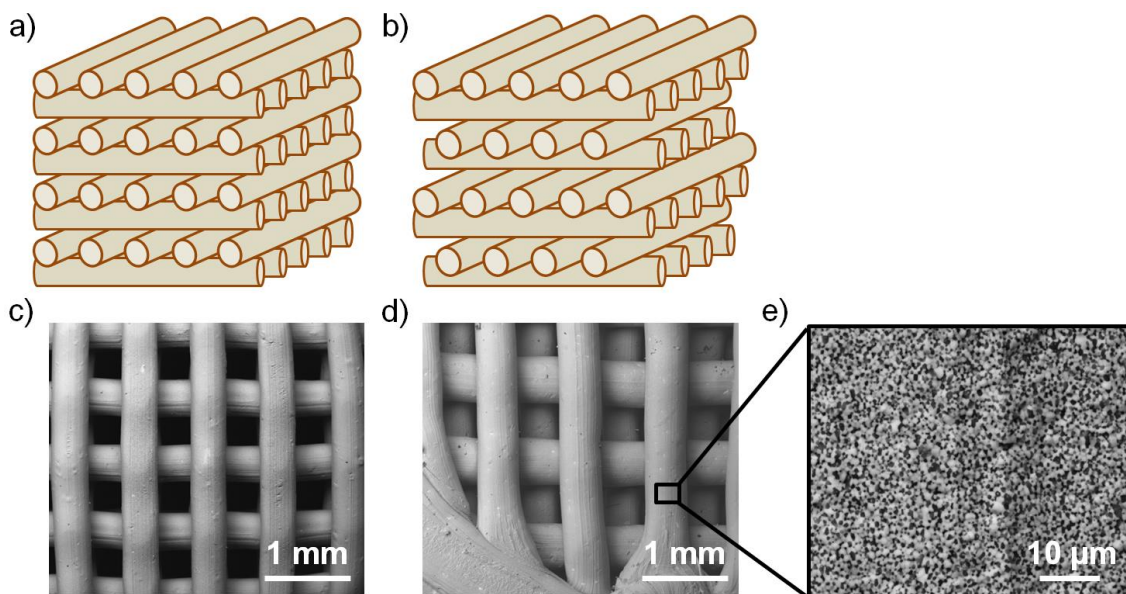


**Fig. 2:** Round lattice design grid configurations: (a) simple pattern and (b) complex pattern. SEM images of (c) a sintered simple round lattice and (d) a sintered complex round lattice, both printed in air through a 580  $\mu\text{m}$  tips. (e) SEM image of the microstructure of a sintered round lattice ink filament.

**Post-processing.** The printed structures were left to dry at room temperature for 24-48 h. Additionally, the dense bars were regularly and gently turned over to aid evaporation in all directions and avoid warping and cracking. Once dry, the printed structures were pre-sintered at 1  $^{\circ}\text{C}/\text{min}$  up to 800  $^{\circ}\text{C}$ , to eliminate organics and allow for up built tension relaxation, and cooled down to 40  $^{\circ}\text{C}$ . **Then, they were once again heated up to 800  $^{\circ}\text{C}$ , this time at a heating rate of 5  $^{\circ}\text{C}/\text{min}$ , before complete sintering at 10  $^{\circ}\text{C}/\text{min}$  up to 1500  $^{\circ}\text{C}$ ,** temperature which was held for 2 h before final cooling (*Table 1*).

**Table 1**

Sintering cycle applied to the 3D printed structures.

Cycle	Ramp	Heating rate (°C/min)	Final temperature (°C)	Holding time (min)
1	1	1	800	0
1	2	free cooling	40	0
2	3	5	800	0
2	4	10	1500	0
2	5	0	1500	120
2	6	free cooling	40	0

## 2.2 Structural characterization of the printed samples

**Density.** The density assessment of the printed structures was performed following the buoyancy method, based on Archimedes' Principle. A Sartorius VRD analytical balance and a Sartorius density determination kit were used to weigh the samples under the appropriate conditions. The density test procedure and evaluation were performed in accordance with European standard EN 993-1 [35].

**Mechanical testing.** The dense rectangular probes were mechanically tested via three-point bending at room temperature, using an Instron 8562 equipped with a 10 kN load cell at a constant rate of 1 mm/min [36]. The bending strengths of the printed bars were compared to those of standard test bars produced by powder mixing, an alternative conventional ceramic processing route. The compression strengths of the porous lattices were obtained using an Instron 5582 equipped with a 100 kN load cell at a crosshead speed of 0.5 mm/min, following the ASTM C133 standard [37].

**Microstructure.** The printed structures were qualitatively studied via scanning electron microscopy (SEM). The FEI Quanta 650 FEG ESEM (INCAR-CSIC, Spain) and the SEM JEOL JSM 5610 LV (Imperial College London, UK) were used depending on image requirements. The samples were finely coated with Au or Ir to improve imaging.

## 2.3 Biological characterization of the printed samples

**Samples.** Three different round lattice designs were tested in vitro: simple round lattices of 200  $\mu\text{m}$  pores, simple round lattices of 600  $\mu\text{m}$  pores and complex round lattices of 600  $\mu\text{m}$  pores. Tissue culture polystyrene (TCPS) was used as the control substrate.

**Cell culture.** Human primary osteogenic sarcoma cells (SAOS-2 cells) were used for in vitro tests. The liquid medium applied to provide the essential nutrients for survival and growth consisted of DMEM medium (GIBCO®, Invitrogen) with glucose (500 mg/l), sodium pyruvate (110 mg/l) and L-glutamine (2 mM) (Sigma Aldrich) supplemented with 10% heat-inactivated fetal calf serum (FCS) (PAA Laboratories GmbH) and 20 U/ml HyClone® penicillin (10000 units/ml) – streptomycin (10000 ug/ml) solution (1  $\mu\text{l/ml}$ ) at 37 °C and 5 % CO<sub>2</sub>.

**Cell viability.** Cell death was evaluated by quantifying the number of living cells in the media. SAOS-2 cells were seeded onto sterilized material samples in 48-well plates at a density of approximately  $1 \times 10^4$  cells/ml. Empty wells, seeded with the same amount of cells, were used as controls (blank). Cell viability was determined after 48 h using the CellTiter 96® AQueous MTS Reagent Powder (Promega). All assays were conducted in triplicate. The quantity of formazan product, as measured by absorbance (Abs) at 490 nm, is directly proportional to the number of living cells in culture. Thus, the % viability was calculated as:  $\% \text{Viability} = 100 \times \text{Abs}_{\text{sample}} / \text{Abs}_{\text{blank}}$ .

**Alkaline phosphatase (ALP) activity determination.** The osseous differentiation ability of the SAOS-2 cells cultured on the porous substrates was evaluated by quantification of ALP activity. SAOS-2 cells were seeded onto sterilized porous substrates in 48-well plates at a density of approximately  $2 \times 10^4$  cells/ml. Empty wells, with the same amount of cells, were used as controls. Cells were incubated for 7 days using supplemented culture medium, replaced every 2-3 days. The osteogenic factors that were added to the cell culture medium were: ascorbic acid (0.2 mM final concentration),  $\beta$ -glycerophosphate (10 mM final concentration) and dexamethasone (0.1  $\mu$ M final concentration) (Sigma Aldrich). ALP activity was determined using the SensoLyte® pNPP Alkaline Phosphatase Assay Kit (AnaSpec Inc.). Absorbance at 405 nm was measured on a BIO-RAD Model 680 Microplate Reader.

**Gene expression quantification.** Gene expression studies were used to quantify the level of expression of specific osseous differentiation-related genes (BGLAP: bone gamma-carboxylglutamate protein, COL1A1: collagen type 1 alpha 1, IBSP: integrin-binding sialoprotein and SPARC: secreted protein acidic and rich in cysteine). A highly conserved protein that is involved in cell motility, structure and integrity, beta-actin (ACTB), was used as the endogenous control for relative gene expression quantification [38]. SAOS-2 cells were seeded onto duplicate sterilized material samples in a 48-well plate at a density of approximately  $5 \times 10^5$  cells/ml and incubated in supplemented culture medium, following the procedure specified for ALP activity determination. RNA was extracted after 7 days of incubation. First of all, the culture medium was removed and 500  $\mu$ l of TRIzol (TRI-Reagent® from Sigma-Aldrich) were added to each well. The 48-well plate, containing the samples and the TRIzol, was frozen for 48 h at  $-80^\circ\text{C}$ . After thawing, the TRIzol solutions were transferred to RNase-free 1.5 ml tubes. 100  $\mu$ l of molecular biology grade 1-Bromo-3-chloropropane (Sigma-Aldrich) were added to each tube, mixed, incubated at room temperature for 3 min and centrifuged at  $12000 \times g$  and  $4^\circ\text{C}$ . The resulting upper aqueous phases were transferred to clean tubes and 250  $\mu$ l of cold ( $4^\circ\text{C}$ ) isopropyl alcohol (Sigma Aldrich) were added to each tube. This solution was incubated for 10 min at room temperature and then centrifuged at  $12000 \times g$  and  $4^\circ\text{C}$  for 10 min. The supernatants were removed and the remaining pellets (RNA) were washed with 500  $\mu$ l of a 75% ethanol solution (obtained by diluting absolute ethanol AnalaR NORMAPUR®, VWR) via centrifugation at  $7500 \times g$  and  $4^\circ\text{C}$  for 5 min. The resulting RNA pellets were dried, without reaching total dehydration, and resuspended in 30  $\mu$ l of PCR grade water (Sigma Aldrich). RNA quantity and purity were obtained by measuring sample absorbance at 260 and 280 nm, using the Thermo Scientific NanoDrop ND-1000 spectrophotometer. Once verified, 500 ng of every total RNA sample were reverse-transcribed in reaction sizes of 20  $\mu$ l to single-stranded cDNA, using the Applied

Biosystems High Capacity cDNA Reverse Transcription Kit and the Bioer's LifePro Thermal Cycler. Finally, we used the Power SYBR® Green PCR Master Mix (Applied Biosystems), the KiCqStart™ SYBR® Green Primers (Sigma Aldrich) (*Table 2*) and 1 µl of each cDNA type (in reaction sizes of 20 µl) for real-time polymerase chain reaction (RT-PCR), which was run at 40 cycles in a 7900HT Fast Real-Time PCR System with a Fast 96-Well Block Module (Applied Biosystems). For statistical purposes, two measurements were made per sample.

**Table 2**

Sigma Aldrich KiCqStart™ SYBR® Green Primers applied for DNA amplification (base pairs = bp).

<b>Oligo Code</b>	<b>T<sub>m</sub>°</b>	<b>Sequence (5'-3')</b>	<b>Sequence Size (bp)</b>
<b>FH1_ACTB</b>	59.7°C	GACGACATGGAGAAAATCTG	131
<b>RH1_ACTB</b>	58.0°C	ATGATCTGGGTCATCTTCTC	
<b>FH1_BGLAP</b>	60.8°C	TTCTTTCCTCTTCCCCTTG	97
<b>RH1_BGLAP</b>	59.3°C	CCTCTTCTGGAGTTTATTTGG	
<b>FH1_COL1A1</b>	61.1°C	GCTATGATGAGAAATCAACCG	199
<b>RH1_COL1A1</b>	61.6°C	TCATCTCCATTCTTTCCAGG	
<b>FH1_IBSP</b>	57.9°C	GGAGACTTCAAATGAAGGAG	80
<b>RH1_IBSP</b>	56.4°C	CAGAAAGTGTGGTATTCTCAG	
<b>FH1_SPARC</b>	52.9°C	AGTATGTGTAACAGGAGGAC	143
<b>RH1_SPARC</b>	57.6°C	AATGTTGCTAGTGTGATTGG	



### 3. Results and discussion

#### 3.1 Ink formulation and rheology

A hydrogel-based 10CeTZP- $\text{Al}_2\text{O}_3$  ink with appropriate rheological properties was developed for 3D deposition. Preliminary experiments and previous work [27] proved that a 25 wt% Pluronic® F-127 stock solution is a suitable carrier for the composite. The ink composition was adjusted to reach optimal flow and structure for 3D printing, attained at 35 vol% ceramic powder and 65 vol% Pluronic® F-127 solution at room temperature (25 wt% in deionized water). This ink is highly viscous at rest but flows easily under shear. At rest it shows viscoelastic behaviour with a predominant elastic component ( $G' > G''$ , Figure 3) and high  $G'$  values (around 10 MPa). Under shear, as will be seen later, the ink network breaks down easily but quickly recovers its initial structure once deposited on the substrate, making the 3D printing process in air possible without the need for supporting structures.

The thermoresponsive behaviour of the Pluronic® F-127 solution is clearly illustrated in its temperature ramp (Fig. 3); its structure goes from solid-like ( $G' > G''$ ), where the storage modulus ( $G'$ ) dominates with values of around 10 kPa, to liquid-like ( $G'' > G'$ ) at low values of  $G'$  ( $< 1$  Pa) with a considerable drop of both moduli (Fig. 3). This is due to the transition temperature of the hydrogel (at  $\sim 17^\circ\text{C}$ ), which becomes liquid at low temperatures. However, the ink does not show the same behaviour with temperature ( $17^\circ\text{C}$ ) (Fig. 3). This is because the ink is a complex system with a high concentration of ceramic particles, resulting in a stiff structure with  $G'$  values of up to 10 MPa. The ink moduli ( $G'$ ,  $G''$ ) do not significantly change with temperature;  $G'$  dominates throughout the tested temperature range, due to the small contribution of F-127 to the total stiffness of the ink ( $G'$  of F-127 25wt% is around 10kPa) (Fig. 3).

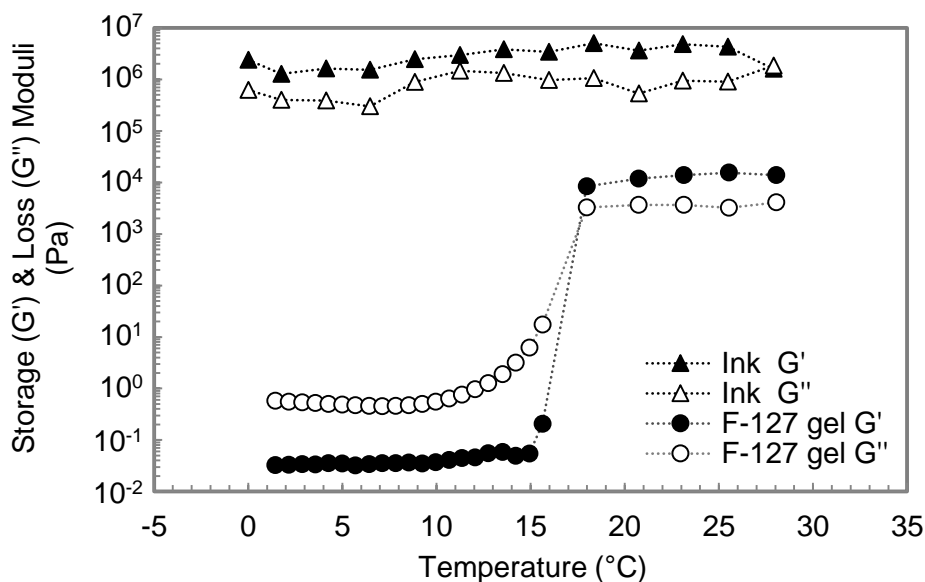


**Fig. 3:** Temperature sweeps illustrating and comparing the behaviour of the ceramic ink and the F-127 solution with temperature. The ink moduli do not change significantly with temperature; the ink's stiff structure causes  $G'$  to dominate throughout the tested temperature range, reaching values close to 10 MPa. However, we can appreciate a

clear change in the behaviour of the F-127 solution with temperature: at temperatures below  $\sim 17^\circ\text{C}$  it shows a liquid-like low viscosity behaviour, and, when temperature rises above  $\sim 17^\circ\text{C}$ ,  $G'$  increases up to 10 kPa and dominates over  $G''$ , proving the thermoresponsive behaviour of the hydrogel.

Frequency and amplitude sweeps provide additional structural information. The ink is very sensitive to frequency (Fig. 4), unlike the Pluronic® F-127 solution alone, which shows linear viscoelastic behaviour with frequency (Fig. 4). In the case of the ceramic ink, frequencies above 4 rad/s easily break down its structure. The amplitude sweep performed on the ink shows a linear viscoelastic region (LVR) at strains below 0.02% (Fig. 5). The ink moduli crossover ( $G'=G''$ , showing the transition from solid to liquid) takes place at 0.6%. **These very low strains manage to break down the ink network enabling it to flow through narrow nozzles during the printing process.** In the LVR, at strains below 1%, the  $G'$  and  $G''$  values of the ink (up to 10 MPa) are much higher than those of the Pluronic® F-127 solution alone (around 10kPa) (Fig. 5) due to the strong contribution of the ceramic particles. This stiffness (high values of  $G'$ ) combined with the shear thinning behaviour is what makes this ink excellent for robocasting. F-127 acts as a lubricant and as a carrier, facilitating the flow and establishing a network across the ceramic particles that can be easily broken down to flow under shear and immediately heal and recover its structure when the shear eases off. Once printed, the filaments are strong enough to retain their shape and support the weight of the layers on top without deformation, leading to self-supporting structures.

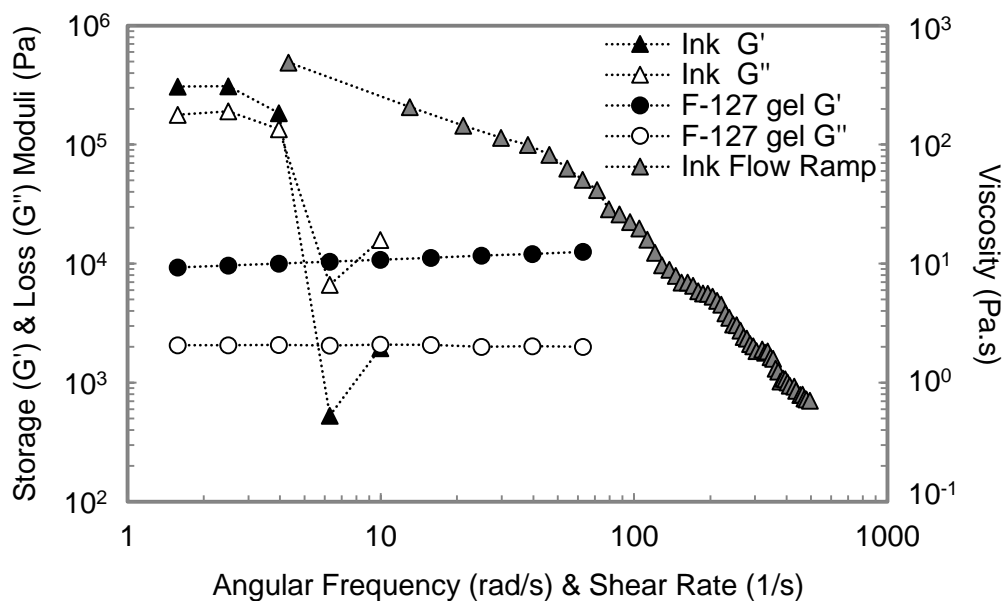


**Fig. 4:** Ceramic ink and F-127 solution (25 wt%) frequency sweeps, at fixed strain (0.1 %), and a Cox-Merz transformation of the ink frequency sweep. The ink is a stiff network that shows shear thinning behaviour and is very sensitive to frequency; frequencies above  $\sim 4$  rad/s break down its structure. Conversely, the Pluronic® F-127 solution shows linear viscoelastic behaviour with frequency.

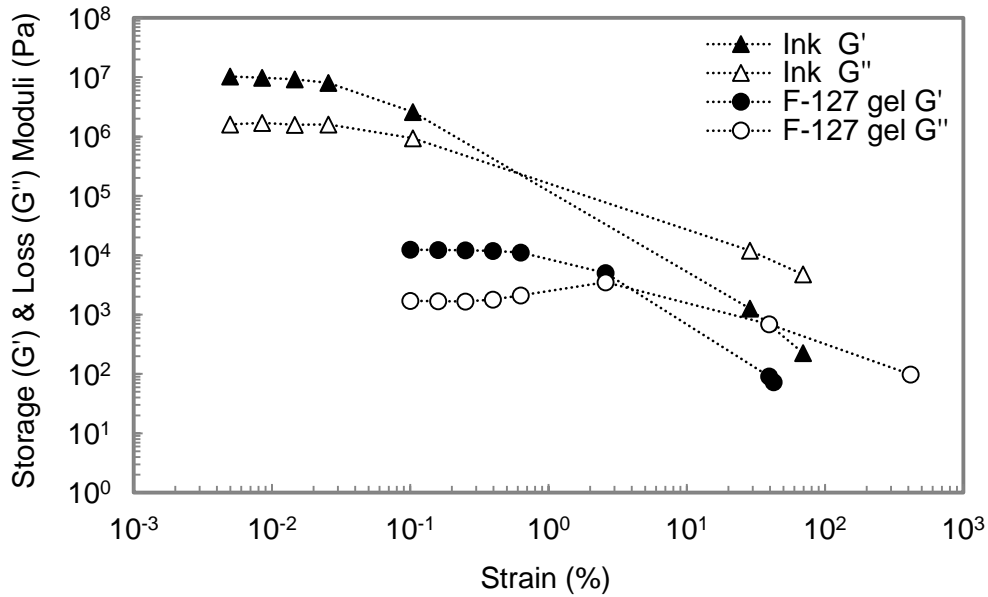


**Fig. 5:** Strain sweep, at fixed frequency (1 Hz), illustrating and comparing the behaviour of the ceramic ink and the F-127 gel with amplitude. The ink shows a linear viscoelastic region (LVR) at strains below 0.02%, while the F-127 solution shows a LVR at strains below 0.6%. The moduli crossover ( $G'=G''$ ) takes place at 0.6% for the ink and at 3% for the F-127 solution. At strains below 1%, the moduli of the ink (up to 10 MPa) are much higher than those of the F-127 solution alone (~10 kPa) due to the strong contribution of the ceramic particles towards the rheological behaviour of the ink.

### 3.2 Robocasting process considerations and parameters

A wide range of 3D designs were printed using the optimised ink formulation (Fig. 1), including rectangular test bars for comparison of their mechanical performance with those made using other conventional processing methods. In this case, the 3D design is critical to guarantee high density within the bars and avoid any defects and voids due to spacing between the filaments, for example. **The design is based on the close superposition of 6 layers; each one consists of a single perimeter rim and a solid space-filling pattern, which is printed perpendicularly to that of the preceding layer (Fig. 6). This configuration allowed us to print a compact structure by minimizing pores and defects that could involve a drop in mechanical property values. The use of conical tips minimized the presence of dead zones along the extrusion path and decreased the extrusion pressure by almost one order of magnitude [30].**

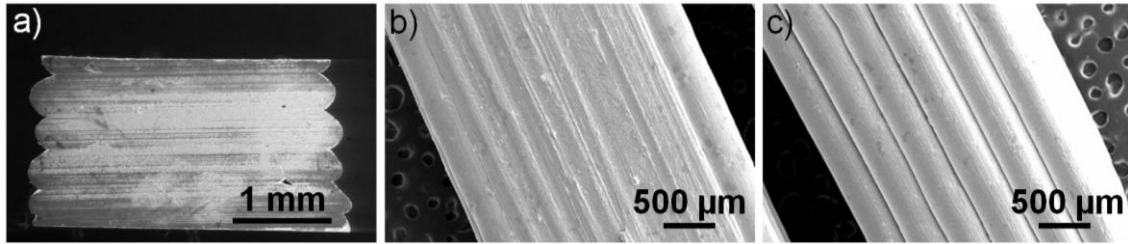


**Fig. 6:** SEM images of a sintered rectangular test bar printed in air through a 580  $\mu\text{m}$  tip. (a) Transversal cut, (b) image taken from the top of the structure and (c) image taken from the side of the structure.

### 3.3 Post-printing processing

Sample drying is a critical processing step and must be carefully controlled to avoid defects such as cracking, distorting and warping, caused by the stresses produced by differential shrinkage [39,40]. Drying defects usually appear when the drying process occurs too fast or unevenly and are especially likely to develop in thick and dense samples. From a set of printing tests on diverse porous and non-porous substrates (mesh-like stainless steel, aluminium foil, newspaper and Teflon) and in different media (air and oil), it was found that the most efficient way to prevent cracking and bending due to uneven drying was printing on a Teflon substrate in air. The most effective drying conditions for the printed samples were found to be drying in air at room temperature (20  $^{\circ}\text{C}$ , approximately) for 24-48 h. Additionally, the dense rectangular bars were turned over extremely carefully, from time to time, to aid evaporation in all directions.

Likewise, the sintering conditions had to be carefully defined to avoid destabilization of the composite material due to spontaneous tetragonal-monoclinic zirconia phase transition, which can cause sample cracking and critical failure. Completely sintered samples, without signs of cracking, distorting or warping were obtained when applying a two-step sintering cycle consisting of two distinct but complimentary heat treatments; the first one was applied to slowly pre-sinter the material, eliminate organics and allow for up built tension relaxation before complete sintering during the second treatment (Table 1).

### 3.4 Printed structure characterization

Dense and porous 3D architectures were successfully printed and sintered. The densities of the rectangular bars (Fig. 6) varied between 92 and 97%. The average  $\sigma_f$  value obtained from 10 bars by three point bending was 408 MPa, which corresponds to 58% of the conventionally processed 10CeTZP- $\text{Al}_2\text{O}_3$   $\sigma_f$  value, 700 MPa [22,23]; the maximum  $\sigma_f$  value reached was 575 MPa, which corresponds to 82% of the conventionally processed 10CeTZP- $\text{Al}_2\text{O}_3$   $\sigma_f$  value [22,23]. No direct correlation appears to exist between the density of the samples and the  $\sigma_f$  value obtained in each specific case. Thus, the lower  $\sigma_f$  values may be due to the existence of random critical flaws in some of the samples, such as isolated pores and superficial defects (Fig. 6a.). Some of these imperfections could be due to remaining air bubbles in the ink, which is also highly

likely to be the reason behind the samples having densities below theoretical for this composite.

3D freestanding porous structures with round lattice designs and interconnected pore networks were successfully fabricated. They all matched the CAD design showing no, or very slight, bending of the ink filaments, which retained their shape across spans of 200-600  $\mu\text{m}$  (*Fig. 2c & 2d*). The external surfaces of the printed filaments after sintering have a very homogeneous microstructure (*Fig. 2e*). The porous designs selected for mechanical and in vitro evaluation have porosities between 32 and 50%, average mechanical strengths in compression ranging from 32 to 178 MPa and Young's modulus values of 0.4 – 1.7 GPa (*Fig. 7a*). As expected, compression strengths decrease as porosity increases. The compression strength values of the simple round lattices of 200  $\mu\text{m}$  pores fall inside the compression strength range reported for cortical bone [41-43]; moreover, the compression strength values of the tested samples are, in every case, noticeably higher than those reported for tricalcium phosphate (TCP)-based 3D printed scaffolds of similar porosities [34]. Comparing the simple and complex round lattice patterns in terms of compressive strength, for the same pore size (600  $\mu\text{m}$ ), porosity (~50%) and ink filament thickness (580  $\mu\text{m}$ ), we find that the complex pattern (~43 MPa) is 34% more robust than the simple pattern (~32 MPa) (*Fig. 7a*). Finally, the stress-strain curve shows that the printed structures can reach high strain values (20-30%), attributed in part to the material's inherent plasticity but mainly to its staggered architecture, which causes it to break down gradually, rather than catastrophically, under stress (*Fig. 7b*).

a)

b)

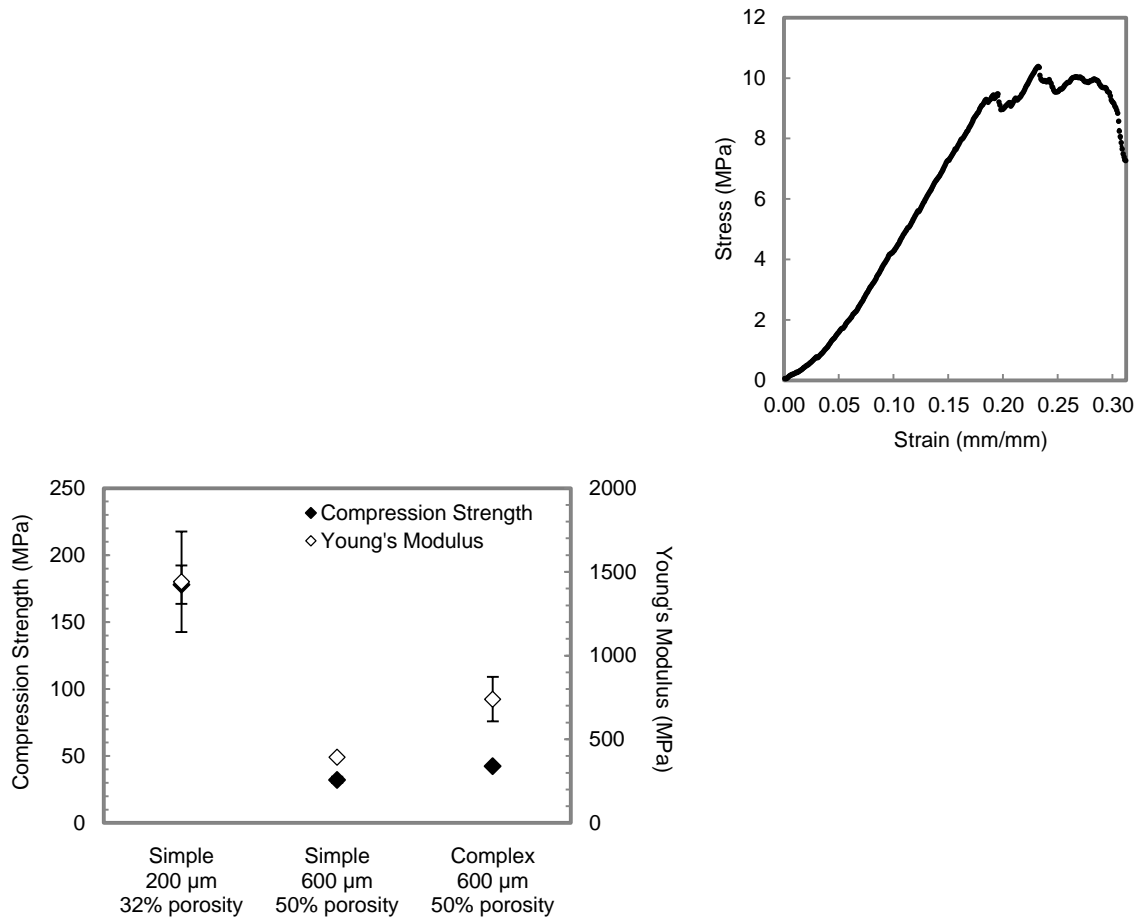


**Fig. 7:** (a) Average compression strength and Young's moduli values of the round lattice designs used for biological testing, all of them printed in air through 580 μm tips. Each value represents the average of three measurements. Sample names indicate their internal pattern, pore size and porosity. The error bars represent standard deviation values. (b) Stress-strain curve of one of the simple lattice designs with 200 μm pores. The corresponding elastic modulus is 2.16 GPa, which confirms the elasticity of the porous structure. Sample failure is gradual, as opposed to catastrophic.

### 3.5 In-vitro biological characterization of the printed samples

In-vitro assay results lead us to believe that our 3D printed composite structures can be considered suitable for biological applications.

A material is considered non-cytotoxic when it allows for over 70% cell viability, as specified in ISO 10993-5 [44]. Cytotoxic effects were analysed by quantifying the number of living cells in the media after culturing SAOS-2 cells for 48 h on the 3D printed samples. None of the tested structures induced sufficient cell death to be considered cytotoxic (Table 3); in fact, they all allowed for almost 100% cell viability.

ALP levels increase when active bone formation (osseous differentiation) is occurring as ALP is a by-product of this process. pNPP (p-Nitrophenyl phosphate) is a chromogenic substrate for ALP and can be used to detect its activity in biological

samples. Upon dephosphorylation, pNPP turns yellow and can be detected by measuring absorbance at 405 nm. Therefore, the amount of osseous differentiation achieved on our ceramic scaffolds, after incubating SAOS-2 cells on the printed structures for 7 days in supplemented culture medium, was evaluated by measuring sample absorbance at 405 nm after the enzymatic reaction with pNPP. The level of ALP activity present on and/or inside the 3D printed samples after the 7 days of incubation is shown in *Table 3*. The simple round lattices seem to induce **more osseous differentiation than the complex ones**, possibly due to them allowing a more efficient cell and medium penetration, **which favours** cell proliferation and subsequent differentiation.

**Table 3**

**Percentage viability of SAOS-2 cells after incubation during 48 h on TCPS and the 3D printed structures and ALP expression (OD<sub>405</sub>) achieved after SAOS-2 incubation during 7 days on the surfaces of TCPS and the 3D printed structures. Sample names indicate their internal pattern and their pore size.**

<b>Sample</b>	<b>Cell viability (%)</b>	<b>ALP expression (OD<sub>405</sub>)</b>
TCPS (control)	100 ± 0.8	0.70 ± 0.05
Simple_200µm	98.7 ± 0.5	0.49 ± 0.11
Simple_600µm	98.9 ± 0.3	0.50 ± 0.01
Complex_600µm	98.6 ± 1.0	0.19 ± 0.01

Polymerase chain reaction (PCR) is the most sensitive and reliable method for the detection and quantification of nucleic acid (DNA, cDNA and RNA) levels [22]. We used real-time PCR to determine the degree of osseous differentiation reached on TCPS (control substrate) and on the scaffolds that had shown the highest compression strength and ALP activity values (simple 200 µm pores) by measuring the relative quantities of specific osseous differentiation genes (BGLAP, COL1A1, IBSP and SPARC) after incubating SAOS-2 cells on the substrates for 7 days in supplemented culture medium. The 3D printed simple round lattice with 200 µm pores shows an increase in the expression of COL1A1, IBSP and SPARC with respect to TCPS while the expression of BGLAP was recorded to be very similar in both cases (*Fig. 8*). These results lead us to believe that the stage of osseous differentiation reached by the SAOS-2 cells on these 3D printed structures is more advanced than that reached on TCPS after the same time of incubation. The early stage differentiation genes, COL1A1 and SPARC [45,46], show more expression than the late stage differentiation genes, BGLAP and IBSP [46,47]; however, both final stage osseous differentiation makers do show some expression, which indicates that the cells are reaching the final stage of osseous differentiation.

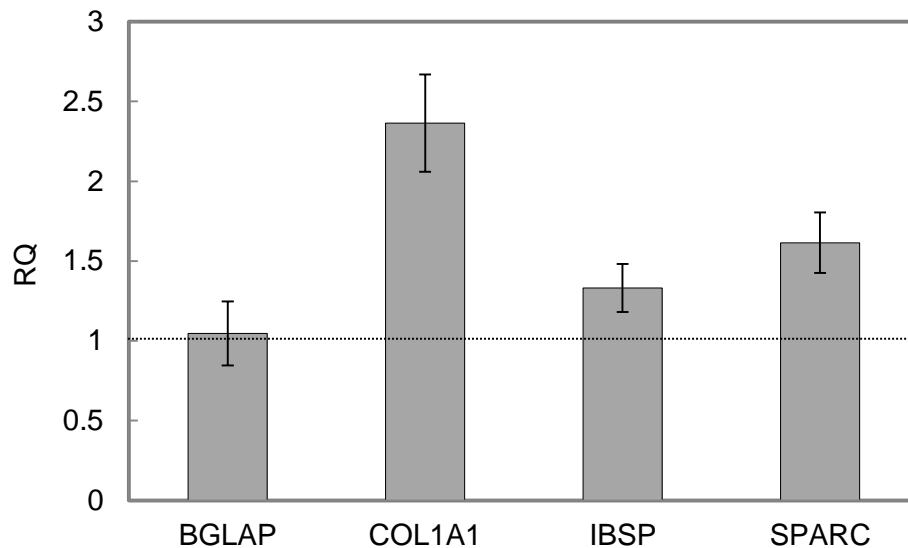


**Fig. 8:** Relative quantities (RQ) of BGLAP, COL1A1, IBSP and SPARC found on TCPS (control measurement, RQ=1) and on the simple round lattice structures with 200  $\mu\text{m}$  pores after SAOS-2 incubation for 7 days. We can appreciate an increase in the expression of COL1A1, IBSP and SPARC on the printed structures with respect to TCPS, while the expression of BGLAP is very similar in both cases. Sample names indicate their internal pattern and pore size. The error bars represent standard deviation values.

#### 4. Conclusions

A printable ceramic ink was developed from 10CeTZP- $\text{Al}_2\text{O}_3$  powder and a hydrogel. Robust three-dimensional ceramic structures were successfully printed, including different round lattice designs with interconnected pores, rectangular bars and cones. The selected round lattice structures showed compression strength values similar to those of cortical bone. The maximum flexural strength value recorded for the dense rectangular bars was 575 MPa, which is 82% of the conventionally processed 10CeTZP- $\text{Al}_2\text{O}_3$   $\sigma_f$  value. In vitro tests demonstrated that none of the printed samples can be considered cytotoxic and, furthermore, that the round lattices induced more osseous differentiation than tissue culture polystyrene.

In summary, porous robocasted 10CeTZP- $\text{Al}_2\text{O}_3$  structures show good mechanical and biological performance in addition to their good aesthetics, chemical stability and negligible corrosion and wear. Therefore, they could be considered for the production of bone scaffolds for load bearing applications, as they can provide the required structural integrity during the osseous integration process.

#### Acknowledgements

This research has been supported by the Spanish Ministry of Science and Innovation (MICINN) and the Spanish Higher Council for Scientific Research (CSIC) under the Project MAT2012-38645. Likewise, the work was partially carried out within the framework of the Regulation of the Government of the Russian Federation dated 9 April



2010 No. 220 (Agreement No. 14.B25.31.0012 dated 26 June 2013). Lidia Goyos-Ball acknowledges financial support from the JAE-PREDOC program (CSIC). Esther García-Tuñón and Eduardo Saiz would like to acknowledge the EPSRC Grant graphene 3D networks (EP/K01658X/1).

## References

1. David A. Puleo RB (2009) *Biological Interactions on Materials Surfaces: Understanding and Controlling Protein, Cell and Tissue Responses*. New York: Springer-Verlag New York.
2. Ivanova EP, Bazaka K, Crawford RJ (2014) *New Functional Biomaterials for Medicine and Healthcare*. 1-226 p.
3. Agel J, Akesson K, Amadio PC, Anderson M, Badley E, et al. (2003) The burden of musculoskeletal conditions at the start of the new millennium. World Health Organization - Technical Report Series. pp. i-218.
4. Bishop JA, Palanca AA, Bellino MJ, Lowenberg DW (2012) Assessment of compromised fracture healing. *Journal of the American Academy of Orthopaedic Surgeons* 20: 273-282.
5. Ratner BD, Hoffman AS, Schoen FJ, Lemons JE (2013) *Introduction - Biomaterials Science: An Evolving, Multidisciplinary Endeavor*. Biomaterials Science (Third Edition): Academic Press. pp. xxv-xxxix.
6. Ratner BD (1996) *Biomaterials Science: An Interdisciplinary Endeavor*. Biomaterials Science. San Diego: Academic Press. pp. 1-8.
7. Chiara G, Letizia F, Lorenzo F, Edoardo S, Diego S, et al. (2012) Nanostructured biomaterials for tissue engineered bone tissue reconstruction. *International Journal of Molecular Sciences* 13: 737-757.
8. George A, Ravindran S (2010) Protein templates in hard tissue engineering. *Nano Today* 5: 254-266.
9. Cabal B, Alou L, Cafini F, Couceiro R, Sevillano D, et al. (2014) A new biocompatible and antibacterial phosphate free glass-ceramic for medical applications. *Scientific Reports* 4.
10. Cheng A, Humayun A, Cohen DJ, Boyan BD, Schwartz Z (2014) Additively manufactured 3D porous Ti-6Al-4V constructs mimic trabecular bone structure and regulate osteoblast proliferation, differentiation and local factor production in a porosity and surface roughness dependent manner. *Biofabrication* 6.
11. Connell LS, Romer F, Suárez M, Valliant EM, Zhang Z, et al. (2014) Chemical characterisation and fabrication of chitosan-silica hybrid scaffolds with 3-glycidoxypropyl trimethoxysilane. *Journal of Materials Chemistry B* 2: 668-680.
12. Esteban-Tejeda L, Zheng K, Prado C, Cabal B, Torrecillas R, et al. (2016) Bone tissue scaffolds based on antimicrobial SiO<sub>2</sub>-Na<sub>2</sub>O-Al<sub>2</sub>O<sub>3</sub>-CaO-B<sub>2</sub>O<sub>3</sub> glass. *Journal of Non-Crystalline Solids* 432: 73-80.
13. Yang JZ, Sultana R, Hu XZ, Ichim P (2014) Novel layered hydroxyapatite/Tri-calcium phosphate-zirconia scaffold composite with high bending strength for load-bearing bone implant application. *International Journal of Applied Ceramic Technology* 11: 22-30.
14. Zizzari VL, Zara S, Tetè G, Vinci R, Gherlone E, et al. Biological and clinical aspects of different bone substitutes integration in oral surgery: a literature review. *Oral Surgery, Oral Medicine, Oral Pathology and Oral Radiology*.
15. Tanaka K, Tamura J, Kawanabe K, Nawa M, Oka M, et al. (2002) Ce-TZP/Al<sub>2</sub>O<sub>3</sub> nanocomposite as a bearing material in total joint replacement. *Journal of Biomedical Materials Research* 63: 262-270.
16. Ritchie RO (2011) The conflicts between strength and toughness. *Nature Materials* 10: 817-822.

17. Fischer J, Stawarczyk B, Trottmann A, Hämmerle CHF (2009) Impact of thermal properties of veneering ceramics on the fracture load of layered Ce-TZP/Al<sub>2</sub>O<sub>3</sub> nanocomposite frameworks. *Dental Materials* 25: 326-330.
18. Fischer J, Stawarczyk B (2007) Compatibility of machined Ce-TZP/Al<sub>2</sub>O<sub>3</sub> nanocomposite and a veneering ceramic. *Dental Materials* 23: 1500-1505.
19. Cutler RA, Mayhew RJ, Prettyman KM, Virkar AV (1991) High-toughness Ce-TZP/Al<sub>2</sub>O<sub>3</sub> ceramics with improved hardness and strength. *Journal of the American Ceramic Society* 74: 179-186.
20. Mangalaraja RV, Chandrasekhar BK, Manohar P (2003) Effect of ceria on the physical, mechanical and thermal properties of yttria stabilized zirconia toughened alumina. *Materials Science and Engineering A* 343: 71-75.
21. Chevalier J, Gremillard L (2009) Ceramics for medical applications: A picture for the next 20 years. *Journal of the European Ceramic Society* 29: 1245-1255.
22. Palmero P, Fornabaio M, Montanaro L, Reveron H, Esnouf C, et al. (2015) Towards long lasting zirconia-based composites for dental implants: Part I: Innovative synthesis, microstructural characterization and invitro stability. *Biomaterials* 50: 38-46.
23. Nawa M, Nakamoto S, Sekino T, Niihara K (1998) Tough and Strong Ce-TZP/Alumina Nanocomposites Doped with Titania. *Ceramics International* 24: 497-506.
24. El Attaoui H, Saâdaoui M, Chevalier J, Fantozzi G (2006) Crack propagation behavior of alumina with different grain sizes under static and cyclic fatigue. *Key Engineering Materials*. pp. 449-452.
25. Deville S, Guénin G, Chevalier J (2004) Martensitic transformation in zirconia: Part I. Nanometer scale prediction and measurement of transformation induced relief. *Acta Materialia* 52: 5697-5707.
26. Jin X-J (2005) Martensitic transformation in zirconia containing ceramics and its applications. *Current Opinion in Solid State and Materials Science* 9: 313-318.
27. Feilden E, Blanca EGT, Giuliani F, Saiz E, Vandeperre L (2016) Robocasting of structural ceramic parts with hydrogel inks. *Journal of the European Ceramic Society* 36: 2525-2533.
28. Munch E, Franco J, Deville S, Hunger P, Saiz E, et al. (2008) Porous ceramic scaffolds with complex architectures. *JOM* 60: 54-59.
29. Smay JE, Gratson GM, Shepherd RF, Cesarano Iii J, Lewis JA (2002) Directed colloidal assembly of 3D periodic structures. *Advanced Materials* 14: 1279-1283.
30. Franco J, Hunger P, Launey ME, Tomsia AP, Saiz E (2010) Direct write assembly of calcium phosphate scaffolds using a water-based hydrogel. *Acta Biomaterialia* 6: 218-228.
31. García-T̂On E, Barg S, Franco J, Bell R, Eslava S, et al. (2015) Printing in three dimensions with Graphene. *Advanced Materials* 27: 1688-1693.
32. Fu Q, Saiz E, Tomsia AP (2011) Direct ink writing of highly porous and strong glass scaffolds for load-bearing bone defects repair and regeneration. *Acta Biomaterialia* 7: 3547-3554.
33. Torrecillas R, Díaz LA (2011) Nanostructured composite material of stabilized zirconia with cerium oxide and doped alumina with zirconia, use, and procedure for obtaining same.
34. Bose S, Vahabzadeh S, Bandyopadhyay A (2013) Bone tissue engineering using 3D printing. *Materials Today* 16: 496-504.
35. AENOR (1996) Methods of test for dense shaped refractory products. Part 1: Determination of bulk density, apparent porosity and true porosity.
36. AENOR (2015) Dentistry - Ceramic materials (ISO 6872:2015) (Endorsed by AENOR in August of 2015).
37. International A (2015) Standard Test Method for Monotonic Compressive Strength of Advanced Ceramics at Ambient Temperature. West Conshohocken, PA.
38. ACTB Gene (Protein Coding) Actin, Beta. Gene Cards - Human Gene Database: Gene Cards Suite.
39. Reed JS (1995) Principles of Ceramics Processing. New York: Wiley-Interscience

40. Bartel M How to Avoid Warped or Cracked Handmade Ceramic Tile. Goshen College Art Department.
41. Bankoff ADP (2012) Biomechanical Characteristics of the Bone. In: Goswami DT, editor. Human Musculoskeletal Biomechanics: InTech.
42. Myer K (2003) Bone Mechanics. Standard Handbook of Biomedical Engineering & Design: McGraw Hill Professional, Access Engineering.
43. Cambridge Uo (2006) Structure of Bone and Implant Materials - Mechanical Properties of Bone. DoITPoMS - Teaching & Learning Packages: University of Cambridge.
44. AENOR (2009) Biological evaluation of medical devices -- Part 5: Tests for in vitro cytotoxicity.
45. Twine NA, Chen L, Pang CN, Wilkins MR, Kassem M (2014) Identification of differentiation-stage specific markers that define the ex vivo osteoblastic phenotype. Bone 67: 23-32.
46. Birmingham E, Niebur GL, McHugh PE, Shaw G, Barry FP, et al. (2012) Osteogenic differentiation of mesenchymal stem cells is regulated by osteocyte and osteoblast cells in a simplified bone niche. European Cells and Materials 23: 13-27.
47. Keselowsky BG, Collard DM, García AJ (2005) Integrin binding specificity regulates biomaterial surface chemistry effects on cell differentiation. Proceedings of the National Academy of Sciences of the United States of America 102: 5953-5957.